JOURNAL OF GEOPHYSICAL RESEARCH, VOL. 103, NO. C3, PAGES 5331–5346, MARCH 15, 1998

# Evolution of mixed Rossby gravity waves

Dennis W. Moore
Pacific Marine Environmental Laboratory, NOAA, Seattle, Washington

R. C. Kloosterziel
School of Ocean and Earth Science and Technology, University of Hawaii, Honolulu

William S. Kessler
Pacific Marine Environmental Laboratory, NOAA, Seattle, Washington

**Abstract.** A Green's function is derived, which can be used to study and predict the evolution of the velocity and pressure fields associated with the mixed Rossby gravity wave component of the totality of motions due to forcing on an equatorial $\beta$ plane. Initial value problems can also be solved with the aid of the Green's function. Since energy associated with the Rossby gravity mode always travels east, the Green's function can be employed to predict what signal should arrive to the east of a given location if the time history of the fields are known at that position. Various simple analytical examples are discussed. A numerical ocean general circulation model is used to demonstrate the usefulness of the Green's function formalism.

## 1. Introduction

Equatorially trapped waves are ubiquitous in observations and solutions to ocean models, and their relatively simple dispersion properties often allow prompt recognition of the signatures of these waves in various observed and modeled fields. This is particularly true for the large-scale, low-frequency equatorial Kelvin and Rossby waves that have been found to form an important part of how the ocean evolves in response to climate signals. The mixed Rossby gravity, or Yanai, wave has been observed and modeled on occasion, but this wave can develop rather complex signals that may prove difficult to interpret. The present paper provides a formalism to define the evolution of the wave fields due to a particular forcing or initial condition.

The linear theory of equatorially trapped oceanic waves began with the work of *Matsuno* [1966] and *Blandford* [1966]. Matsuno obtained the dispersion relation and, for vertically standing modes, demonstrated the completeness of the horizontal modes, which are Hermite functions. Thus the initial value problem for free waves in a horizontally unbounded domain could be solved. Later work turned to the effects of boundaries [*Moore,* 1968] and forcing by wind [*Lighthill,* 1969]. *McCreary* [1981] produced a steady linear theory for the undercurrent, with dissipative terms taking the place of time dependence. *Cane and Sarachik* [1976, 1977, 1981] and *McCreary* [1976, 1983, 1984, 1985] refined the theory and investigated a number of idealized problems.

Mixed Rossby gravity waves have been observed in all three equatorial oceans. *Ripa and Hayes* [1981] argued that antisymmetric variability from a Galapagos pressure array was dominated by mixed Rossby gravity waves with periods in the 10–20-day range. *Enfield et al.* [1987] supported this conclusion. *Weisberg and Horigan* [1981] observed vertically propagating oscillations of meridional current at depths to 2000 m in the Gulf of Guinea, which they identified as the signatures of mixed Rossby gravity waves generated by instabilities of the surface zonal currents. In the introduction to a paper on a 26-day oscillation, *Tsai et al.* [1992] reviewed both the available observations and modeling efforts with respect to the mixed Rossby gravity wave in the equatorial Indian Ocean. *Luyten and Roemmich* [1982] found a 26-day oscillation in the meridional velocity in the upper 200 m at 55°E. *Reverdin and Luyten* [1986] inferred the existence of the mixed Rossby gravity waves from drifter data, and *Tsai et al.* [1992] found clear evidence for a 26-day oscillation in satellite sea surface temperature (SST) measurements.

Several modeling studies have sought to explain these observations. *Kindle and Thompson* [1989] drove a nonlinear model with monthly mean winds and found a 26-day oscillation, attributed by them to an instability. *Moore and McCreary* [1990] tried a linear model with sloping coastline to convert the effect of oscillating zonal winds into waves with meridional flow across the equator. But with no clear 26-day peak in the wind, it is not clear that this mechanism is relevant to the Indian Ocean observations.



Paper number 97JC02419.
0148-227/98/97JC-02419$09.00

For each vertical normal mode, characterized by a Kelvin wave speed $c$, the mixed Rossby gravity wave dispersion is $k = \omega/c - \beta/\omega$, where $k$ is the horizontal east-west wavenumber, $\omega$ is the frequency, and $\beta = 2\Omega/R$ is the equatorial value of *Rossby's* [1939] $\beta$ parameter ($\Omega$ being Earth's rotation rate and $R$ being Earth's radius). Mixed Rossby gravity waves can have a phase velocity in either direction, but the group velocity $c_g$ is always to the east and lies between $c_g = 0$ and $c_g = c$. Thus the mixed Rossby gravity wave signal at any location must have been generated somewhere to the west. The mixed Rossby gravity wave signal at any longitude plus the zonal and meridional winds to the east of that longitude are sufficient to predict the wave signal everywhere to the east of that longitude.

The purpose of the present paper is to cast the theory for the mixed Rossby gravity wave in a form that is useful for testing this predictability. It provides the theoretical basis for testing these ideas against a variety of data sets, both from observations and from models. In section 2 we briefly discuss the equations governing linear internal equatorial waves and the projection of the dynamics on vertical normal modes and Hermite functions in the north-south direction. Then we derive the equations governing the mixed Rossby gravity wave dynamics. We derive the Green's function for the mixed Rossby gravity wave in physical $(x, t)$ space ($x$ denotes longitude, $t$ denotes time) through Laplace transform methods. Some analytical examples are worked out explicitly in section 3 to illustrate the effects of mixed Rossby gravity wave dispersion. In section 3.3 a numerical ocean general circulation model is used to test the applicability of the Green's function formalism. Section 4 summarizes the main results, while the Appendix discusses the Green's function formulation in spectral form, which can sometimes be useful in solving particular initial value problems.

## 2. Equations of Motion

We consider forced linear hydrostatic motions of an incompressible rotating stratified Boussinesq fluid in a horizontally unbounded ocean of constant depth $H$. Their governing equations are

$$\partial_t u - fv + \partial_x p = \tau^x, \quad (1)$$

$$\partial_t v + fu + \partial_y p = \tau^y, \quad (2)$$

$$\partial_z p = b, \quad (3)$$

$$\partial_t b + N^2(z) w = 0, \quad (4)$$

$$\partial_x u + \partial_y v + \partial_z w = 0. \quad (5)$$

Here $u, v$, and $w$ are the zonal, meridional, and vertical velocity components, respectively; $p$ is the pressure (divided by a constant reference density); $f$ is the Coriolis frequency; $b$ is the buoyancy; and $N^2(z)$ is the Brunt-Väisälä or buoyancy frequency. The terms on the right-hand side of (1) and (2) represent body forces acting in the $x$ and $y$ direction, respectively. The surface is at $z = 0$, and the bottom is at $z = -H$. In the present paper we will only consider the internal adjustment process due to the dispersion of the relatively slow internal modes and not the external adjustment due to the dispersion of the fast external surface mode. Thus we use the boundary conditions

$$w = 0, \quad z = -H, 0. \quad (6)$$

The present study concerns the dynamics of forced motion in the equatorial regions, and we will make the equatorial $\beta$ plane approximation; that is, the Coriolis parameter in (1) and (2) is $f = \beta y$ with $y$ being the distance from the equator.

We expand the fields in usual vertical normal modes $\phi_n(z)$ [see, e.g., *Gill*, 1982]

$$(u, v, p, \tau^x, \tau^y) = \sum_{n=1}^{\infty} (u_n, v_n, p_n, \tau_n^x, \tau_n^y)\phi_n(z),$$
$$w = \frac{1}{N^2(z)} \sum_{n=1}^{\infty} w_n \frac{d}{dz}\phi_n(z), \quad (7)$$

where the $\phi_n$ are eigenfunctions (with eigenvalues $c_n^{-2}$) of the Sturm-Liouville problem

$$\frac{d}{dz}\left[\frac{1}{N^2(z)}\frac{d}{dz}\phi_n\right] + \frac{1}{c_n^2}\phi_n = 0,$$

with boundary conditions

$$\left.\frac{d\phi_n}{dz}\right|_{z=-H,0} = 0.$$

The gravity wave speed $c_n$ for the $n$th vertical normal mode is often written as $c_n = \sqrt{gh_n}$, where $h_n$ is the equivalent depth for the $n$th baroclinic mode. The magnitude of $c_n$ decreases monotonically with increasing mode number $n$. Substitution of the expansions in (1)–(5) leads, after projection on mode $n$ and elimination of the buoyancy and vertical velocity between the equations, to the set of shallow water equations

$$\partial_t u_n - \beta y v_n + \partial_x p_n = \tau_n^x, \quad (8)$$

$$\partial_t v_n + \beta y u_n + \partial_y p_n = \tau_n^y, \quad (9)$$

$$c_n^{-2}\partial_t p_n + \partial_x u_n + \partial_y v_n = 0. \quad (10)$$

It will be convenient to nondimensionalize (8)–(10). We choose a length scale $L_n$ for $x, y$ and a timescale $T_n$ for $t$ defined by

$$L_n = \sqrt{\frac{c_n}{\beta}}, \quad T_n = \frac{1}{\sqrt{\beta c_n}}, \quad (11)$$

and some velocity scale $U$ for $u, v$. Pressure is scaled with $Uc_n$, and the forcing is scaled with $U/T_n$. The nondimensional equations are then the same as (8)–(10) but with $c_n = \beta = 1$. In what follows we will for the sake of convenience drop the index $n$. Note that since the $c_n$ decrease with increasing $n$, the timescale $T_n$ increases with $n$. Thus the evolution associated with the first baroclinic mode $n = 1$ is the fastest.

### 2.1. Mixed Rossby Gravity Waves

The following equation for $v$ alone can be derived from (8)–(10) through cross-differentiation

$$\partial_t(\partial_y^2 - y^2)v + (\partial_t\partial_x^2 + \partial_x)v - \partial_t^3 v = (y\partial_t - \partial_x\partial_y)\tau^x - (\partial_t^2 - \partial_x^2)\tau^y. \quad (12)$$

In order to obtain separable solutions to (12) the $y$ dependence of solutions is resolved in terms of eigenfunctions of the $[(d/dy)^2 - y^2]$-operator. They are Hermite functions $\psi_m(y)$ which satisfy

$$\frac{d^2\psi_m}{dy^2} - y^2\psi_m = -(2m+1)\psi_m, \qquad \psi_m(y) = \frac{e^{-y^2/2}H_m(y)}{\sqrt{2^m m!\sqrt{\pi}}} \quad (m = 0, 1, 2, \cdots). \quad (13)$$

The $\psi_m$ are orthonormal functions; that is, $\int_{-\infty}^{+\infty} \psi_m \psi_n dy = 1$ for $n = m$ and zero otherwise. For even index $m$ the $\psi_m$ are symmetric in $y$ while for odd $m$ they are antisymmetric. For example,

$$\psi_0(y) = \frac{e^{-y^2/2}}{\pi^{1/4}}, \quad \psi_1(y) = \frac{\sqrt{2}ye^{-y^2/2}}{\pi^{1/4}}.$$

Assuming the fields are bounded in the $y$ direction, they can be expanded to

$$\{u, v, p, \tau^x, \tau^y\}(x, y; t) = \sum_{m=0}^{\infty} \{u_m, v_m, p_m, \tau_m^x, \tau_m^y\}(x; t)\psi_m(y) \quad (14)$$

[see *Moore and Philander,* 1976; *McCreary,* 1985].

In order to identify the variety of free waves that can be supported by the system the right-hand side of (12) is set equal to zero (no forcing). For plane waves of the form $v_m(x; t) \propto e^{i(kx-\omega t)}$, substitution in (12) then shows

$$\omega^2 - k^2 - k/\omega - (2m+1) = 0. \quad (15)$$

This can be solved for $k$ in the form

$$k = -\frac{1}{2\omega} \pm \sqrt{\omega^2 + \frac{1}{4\omega^2} - (2m+1)}.$$

For $m = 0$ the two solutions are $k = -\omega$ and $k = \omega - \omega^{-1}$. The first root, a nondispersive westward traveling wave, is disallowed on the unbounded equatorial $\beta$ plane because the corresponding $u$ and $p$ fields become exponentially large as $y$ increases. The second root provides the dispersion relation for the mixed Rossby gravity wave. There are two branches (see Figure 1) given by

$$\omega_\pm(k) = \frac{k}{2} \pm \sqrt{1 + \frac{k^2}{4}}. \quad (16)$$

The horizontal group velocity is

$$c_g = \frac{d\omega}{dk} = \frac{1}{2} \pm \frac{k/4}{\sqrt{1 + k^2/4}}, \quad (17)$$

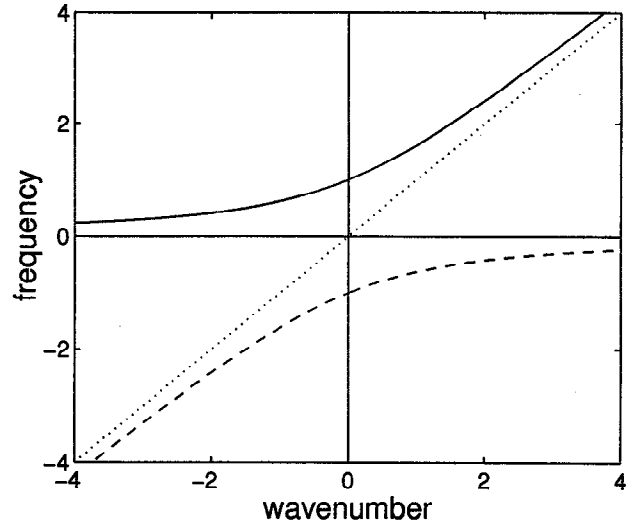


**Figure 1.** Dispersion curves $\omega_\pm(k)$ according to (16). The solid line is $\omega_+$, and the dashed line is $\omega_-$. The dotted line indicates the asymptotic nondispersive behavior at very high wavenumbers, with the maximum group velocity (nondimensionally) $c_g = 1$.

which is positive for any $k$, i.e., toward the east (positive $x$ direction). For both branches the maximum group velocity is $c_g = 1$ and the minimum is $c_g = 0$. Therefore, if we are given an initial disturbance (at time $t = t_0$) at position $x = x_0$, that disturbance will at time $t > t_0$ be found to the east of the initial position, i.e., at $x - x_0 > 0$, but within the region in $x$ space defined by $(t - t_0) - (x - x_0) > 0$ because the finite maximum group velocity implies that in a nondimensional time interval $\Delta t$ the disturbance can at most have traveled a nondimensional distance $\Delta x = \Delta t$ to the east. Note that both the maximum and minimum group velocity are associated with the very high wavenumbers.

The forced mixed Rossby gravity wave meridional velocity field $v$ is obtained by projecting (12) on $\psi_0(y)$. Using the relations [*Wiener,* 1933]

$$y\psi_m = \sqrt{\frac{m+1}{2}}\psi_{m+1} + \sqrt{\frac{m}{2}}\psi_{m-1},$$
$$\frac{d\psi_m}{dy} = -\sqrt{\frac{m+1}{2}}\psi_{m+1} + \sqrt{\frac{m}{2}}\psi_{m-1},$$

we find

$$\partial_t^2 v_0 + \partial_t\partial_x v_0 + v_0 = (\partial_t + \partial_x)\tau_0^y - \tau_1^x/\sqrt{2}, \quad (18)$$

where $\tau_0^y$ and $\tau_1^x$ are the components that occur in the expansions (14). We note that (18) implies that if the zonal forcing $\tau^x$ is symmetric in $y$ and the meridional forcing $\tau^y$ is antisymmetric, no mixed Rossby gravity wave will be excited because then $\tau_1^x = \tau_0^y = 0$.

The $u$ and $p$ fields associated with the mixed Rossby gravity wave are $u = p = u_1(x; t)\psi_1(y)$ with

$$u_1 = (\tau_0^y - \partial_t v_0)/\sqrt{2} \quad (19)$$

and

$$(\partial_t + \partial_x)u_1 = v_0/\sqrt{2} + \tau_1^x/2. \tag{20}$$

Elimination of $v_0$ between (19) and (20) yields

$$\partial_t^2 u_1 + \partial_t \partial_x u_1 + u_1 = \partial_t \tau_1^x/2 + \tau_0^y/\sqrt{2}. \tag{21}$$

For a more complete discussion of these derivations, see *Gill* [1982, section 11.4].

### 2.2. Solutions on an Infinite Domain

Solutions to (18) and (21) can formally be expressed through the use of a Green's function (see the appendix) or with Laplace transform methods. Both techniques lead to the same form of solution. Consider (21) for instance. Assuming that at time $t = t_0$ we know $u_1$ and whichever derivatives of $u_1$ are needed, and the forcing is given for $t \geq t_0$, the natural way to proceed is to employ the Laplace transform. If we define

$$\tilde{u}_1(x;s) = \int_{t_0}^{\infty} e^{-st} u_1(x;t)dt,$$

$$\{\tilde{\tau}_1^x, \tilde{\tau}_0^y\}(x;s) = \int_{t_0}^{\infty} e^{-st}\{\tau_1^x, \tau_0^y\}(x;t)dt,$$

then the Laplace transform of (21) leads to the equation

$$\partial_x \tilde{u}_1(x;s) + \left(s^{-1} + s\right)\tilde{u}_1(x;s) = \left[\frac{v_0(x;t_0)}{s\sqrt{2}} + u_1(x;t_0) + \frac{\tilde{\tau}_1^x(x;s)}{2} + \frac{\tilde{\tau}_0^y(x;s)}{s\sqrt{2}}\right] e^{-st_0}. \tag{22}$$

The solution to (22) is

$$\tilde{u}_1(x;s) = e^{-st_0}\int_{-\infty}^{x} [\cdots] e^{-(s^{-1}+s)(x-x_0)}dx_0, \tag{23}$$

where $[\cdots]$ stands for all the terms occurring within the square brackets on the right-hand side of (22) as a function of the variable $x_0$ instead of $x$. We have used the boundary condition $\tilde{u}_1(x = -\infty; s) = 0$ in deriving (23). This makes physical sense since the group velocity is always toward the positive $x$ direction, and no signal will propagate towards $x = -\infty$. The inverse Laplace transform is given by [*Morse and Feshbach,* 1953]

$$u_1(x;t) = \frac{1}{2\pi i}\int_{c-i\infty}^{c+i\infty} \tilde{u}_1(x;s)e^{st}ds,$$

where the constant $c$ is such that singular points of $\tilde{u}_1(x;s)$ in the complex $s$ plane lie to the left of the contour and $t \geq t_0$. Interchanging the order of integration, we get

$$u_1(x;t) = \int_{-\infty}^{x} \frac{1}{2\pi i}\int_{c-i\infty}^{c+i\infty} \left[\frac{v_0(x_0;t_0)}{s\sqrt{2}} + u_1(x_0;t_0) + \frac{\tilde{\tau}_1^x(x_0;s)}{2} + \frac{\tilde{\tau}_0^y(x_0;s)}{s\sqrt{2}}\right] \cdot e^{s(t-t_0)-(s+s^{-1})(x-x_0)}dsdx_0. \tag{24}$$

The first integral

$$\int_{-\infty}^{x} \frac{v_0(x_0;t_0)}{\sqrt{2}} \frac{1}{2\pi i}\int_{c-i\infty}^{c+i\infty} \frac{e^{s(t-t_0)-(s+s^{-1})(x-x_0)}}{s}dsdx_0$$

is easily determined. For $(t - t_0) - (x - x_0) < 0$ we close the contour in the right hand side of the complex $s$ plane, and since the only singularity is at $s = 0$, the integral is zero. For $(t - t_0) - (x - x_0) > 0$ we can close the contour in the left-hand side of the complex plane. Expanding the essential singularity in the exponent, we find that the integral with respect to $s$ is equal to

$$\frac{1}{2\pi i}\oint \sum_{n=0}^{\infty} \frac{(-1)^n(x-x_0)^n}{n!s^{n+1}} e^{s(t-t_0)-s(x-x_0)}ds = \sum_{n=0}^{\infty} \frac{(-1)^n(x-x_0)^n\left[(t-t_0)-(x-x_0)\right]^n}{n!n!},$$

which is recognized as the expansion of the Bessel function $J_0\left[2\sqrt{x-x_0}\sqrt{(t-t_0)-(x-x_0)}\right]$, where [*Watson,* 1966]

$$J_m(2z) = z^m \sum_{n=0}^{\infty} \frac{(-1)^n z^{2n}}{n!(n+m)!}. \tag{25}$$

Introducing the Heaviside stepfunction $U(x)$, with $U(x < 0) = 0$ and $U(x > 0) = 1$, the integral involving $v_0(x;t_0)$ in (24) is equal to

$$\int_{-\infty}^{+\infty} G(x;t|x_0;t_0)\frac{v_0(x_0;t_0)}{\sqrt{2}}dx_0,$$

where

$$G(x;t|x_0;t_0) = U(x-x_0)U\left[(t-t_0)-(x-x_0)\right] \cdot J_0\left[2\sqrt{x-x_0}\sqrt{(t-t_0)-(x-x_0)}\right]. \tag{26}$$

The integral representation for $G$ is

$$G(x;t|x_0;t_0) = \frac{U(x-x_0)}{2\pi i}\int_{c-i\infty}^{c+i\infty} \frac{e^{s(t-t_0)-(s+s^{-1})(x-x_0)}}{s}dsdx_0. \tag{27}$$

The second integral involving $u_1(x;t_0)$ in (24) is seen to be equal to

$$\int_{-\infty}^{+\infty} u_1(x_0;t_0)\partial_t G(x;t|x_0;t_0)dx_0.$$

Because $\tilde{\tau}_1^x$ and $\tilde{\tau}_0^y$ in (24) are functions of $s$, it follows with the well-known convolution theory for Laplace transforms [*Morse and Feshbach*, 1953] that the integrals involving $\tilde{\tau}_1^x(x;s)$ and $\tilde{\tau}_0^y(x;s)$ are equal to a convolution in time with $G$. Putting everything together, we find that for $t > t_0$

$$\begin{aligned} u_1(x;t) = &\int_{-\infty}^{+\infty} \left[ G(x;t|x_0;t_0)\frac{v_0(x_0;t_0)}{\sqrt{2}} \right. \\ &\left. + \partial_t G(x;t|x_0;t_0)u_1(x_0;t_0) \right] dx_0 \\ &+ \int_{t_0}^{t}\int_{-\infty}^{+\infty} \left[ G(x;t|x_0;t')\frac{\tau_0^y(x_0;t')}{\sqrt{2}} \right. \\ &\left. + \partial_t G(x;t|x_0;t')\frac{\tau_1^x(x_0;t')}{2} \right] dx_0 dt'. \end{aligned} \tag{28}$$

In the same fashion it is found that

$$\begin{aligned} v_0(x;t) = &\\ &\int_{-\infty}^{+\infty} \left\{ G(x;t|x_0;t_0)\left[\partial_{x_0}v_0(x_0;t_0) - \sqrt{2}u_1(x_0;t_0)\right] \right. \\ &\left. + \partial_t G(x;t|x_0;t_0)v_0(x_0;t_0) \right\} dx_0 \\ &+ \int_{t_0}^{t}\int_{-\infty}^{+\infty} \left\{ G(x;t|x_0;t')\left[\partial_{x_0}\tau_0^y(x_0;t') - \frac{\tau_1^x(x_0;t')}{\sqrt{2}}\right] \right. \\ &\left. + \partial_t G(x;t|x_0;t')\tau_0^y(x_0;t') \right\} dx_0 dt'. \end{aligned} \tag{29}$$

Note that in both (28) and (29) the first space integral contains the initial data for the $u_1$ and $v_0$ field, while the second space-time integral is over the forcing.

We have given the kernel appearing in these integrals the symbol $G$ because it is in fact the Green's function for (18) and (21) (see the appendix). The two step-functions $U(x - x_0)$ and $U[(t - t_0) - (x - x_0)]$ in (26) contain the physics derivable from group velocity considerations. No signal travels west; that is, an observer at position $x$ does not receive a signal coming from $x_0$ if $x_0 > x$, and no signal in a time interval $t - t_0$ can reach position $x$ coming from $x_0$ if $x - x_0 > t - t_0$.

In Figure 2 the Green's function is shown at various times $t - t_0 > 0$. It is symmetric about the point $x - x_0 = (t - t_0)/2$ where the amplitude is $J_0(t - t_0)$. The front is at $x - x_0 = t - t_0$. As time increases, more and more oscillations get packed in a narrow $x$ region behind the propagating front, while the inner region has an almost flat amplitude profile, which for large time tends to zero. A same region of rapid oscillations for large times is also found close to the right of the source origin $x - x_0 = 0$. This behavior can be understood through a consideration of the dispersion relation (16), which shows that both the maximum and minimum group velocity (1 and 0, respectively) are at the very high wavenumbers, and the very short scales thus both propagate fastest and stay put as well.

### 2.3. Solutions on a Semi-Infinite Domain

The above formulas were obtained by integrating (22) from $x_0 = -\infty$ to $x$ and using the boundary condition $u_1(x = -\infty;t) = 0$. It will also be useful to consider a semi-infinite domain; that is, $x \in [0, \infty)$. When we integrate (22) from $x_0 = 0$ to $x$, we get (23) again but with the lower limit of integration at $x_0 = 0$ plus an additional term

$$e^{-st_0}\tilde{u}_1(x = 0;s)e^{-(s+s^{-1})x}.$$

The inverse Laplace transform of (23) leads to the same expression as (28) but with integration from $x_0 = 0$ to $x_0 = x$. The inverse Laplace transform of the above additional boundary term is

$$\begin{aligned} &\frac{1}{2\pi i}\int_{c-i\infty}^{c+i\infty} \tilde{u}_1(x = 0;s)e^{s(t-t_0)-(s+s^{-1})x}ds = \\ &\qquad \int_{t_0}^{t} u_1(x = 0;t')\partial_t G(x;t|0;t')dt'. \end{aligned} \tag{30}$$

This expression needs to be added to (28) if a semi-infinite domain is considered. The total solution for $u_1$ is then, as before, determined by the initial conditions in the domain and the time history of the forcing plus the time history of $u_1$ data on the boundary $x = 0$. If we are interested in the case where at $x = 0$, $v_0$ data are prescribed, we find that a term

$$\int_{t_0}^{t} v_0(x = 0;t')\partial_t G(x;t|0;t')dt'$$

needs to be added to (29), while all the spatial integrals run from $x_0 = 0$ onward.

## 3. Examples

### 3.1. Case of Zero Initial Data Plus Time-Dependent Forcing

Here we consider the case where at $t = 0$ both $u_1$ and $v_0$ are zero, and the forcing $\tau_0^y$ is started. We take the case where the forcing is concentrated in a narrow $x$ strip, which we approximate by a $\delta$ function; that is, we take $\tau_0^y$ to be of the form $\tau_0^y(x;t) = \delta(x)f(t)$. The simplest case is where $f(t) = U(t)$; that is, the forcing is switched on at $t = 0$ and is constant in time afterward. In this case the Laplace transform of $\tau_0^y$ is $\tilde{\tau}_0^y = \delta(x)/s$. According to (24) the solution for $t, x > 0$ is

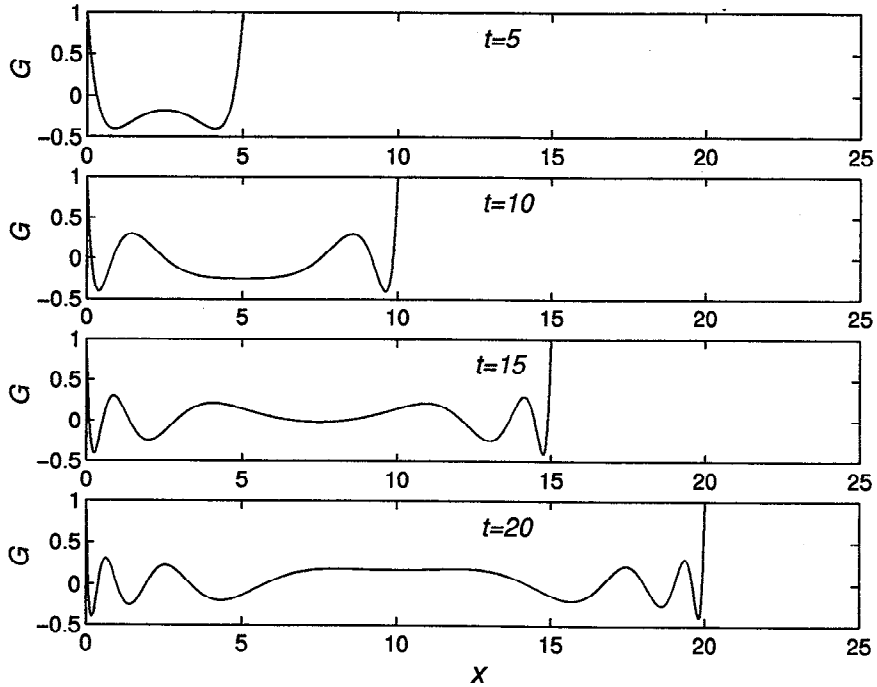


**Figure 2.** The Green's function (26) at four different times as indicated. Without loss of generality, we have put $x_0 = t_0 = 0$.

$$\sqrt{2}u_1(x;t) = \frac{1}{2\pi i}\int_{c-i\infty}^{c+i\infty} \frac{e^{st-(s^{-1}+s)x}}{s^2}ds. \qquad (31)$$

The integrals are similar to (27) with a higher power of $s$ in the divisor. For $t - x > 0$ one gets

$$\sqrt{2}u_1(x;t) = \sum_{n=0}^{\infty} \frac{(-1)^n x^n (t-x)^{n+1}}{n!(n+1)!}$$
$$= \sqrt{\frac{t-x}{x}} J_1(2\sqrt{x}\sqrt{t-x}), \qquad (32)$$

where we have used (25). The $v_0$ response to the switch-on forcing is most rapidly determined by observing that (19) implies that the Laplace transform of $v_0(x;t)$, denoted by $\tilde{v}_0(x;s)$, is related to the Laplace transform of $u_1$ according to

$$\tilde{v}_0(x;s) = -\frac{\sqrt{2}\tilde{u}_1(x;s)}{s} + \frac{\delta(x)}{s}, \qquad (33)$$

where

$$\sqrt{2}\tilde{u}_1(x;s) = \frac{e^{-(s^{-1}+s)x}}{s^2}.$$

When we calculate $(2\pi i)^{-1}\int e^{st}\tilde{v}_0(x;s)ds$, we now find that the second term in (33) simply leads to a contribution $\delta(x)t$, while the first term is similar to the integral (31) but with $s^{-3}$ instead of $s^{-2}$ in it. The series resulting from the expansion about the essential singularity at $s = 0$ is then recognized as a term involving a Bessel function $J_2$ instead of $J_1$. We find

$$v_0(x;t) = -\frac{t-x}{x} J_2(2\sqrt{x}\sqrt{t-x}) + \delta(x)t. \qquad (34)$$

The second term is zero for any $x \neq 0$.

The leading edge of the signal is in both the $u_1$ and the $v_0$ response at $x/t = 1$ (first term in (32) and (34)); that is, it travels at the maximum group velocity. No signal travels to the left of the pulse location; that is, $v_0 = u_1 = 0$ when $x < 0$. Close to $x = 0$, we find that $u_1 \approx t/\sqrt{2}$ and $v_0 \approx -t^2/2$; that is, the $u_1$ field grows linearly in time, and the $v_0$ field grows quadratically. Close to the front ($t - x$ small) and at large times, the amplitudes get very small because of the $1/\sqrt{x}$ and $1/x$ factor multiplying $J_1$ and $J_2$ in (32) and (34), respectively. Unlike in the case of the Green's function, there is no discontinuity at the front; that is, $v_0(x = t;t) = u_1(x = t;t) = 0$. Thus low-amplitude motions propagate east, while near the region of forcing the amplitudes keep increasing. More complicated examples where $f(t)$ is, say, piecewise linear in time can also be solved exactly. But, basically, the same results are found: no discontinuity at the front, low-amplitude propagation to the east, and high-amplitude motion near the forcing region. Similar exact solutions with a simultaneously nonzero $\tau_1^x$ of the form $\delta(x)g(t)$ can easily be found. For forcing of finite size in $x$, things get more complicated, and one has to resort to numerical integration.

The above results can be used to solve the case where the forcing is switched on at $t = 0$ and then switched off at a later time $t = \Delta t$; that is, $\tau_0^y(x;t) = \delta(x)f(t)$

with

$$f(t) = 1, \quad 0 \le t < \Delta t, \qquad f(t) = 0, \quad t > \Delta t. \tag{35}$$

All one has to do is subtract a time-delayed version from (32) and (34), i.e., the expressions given there but with $t$ replaced by $t - \Delta t$. Thus, for $u_1$, one gets

$$\sqrt{2}u_1(x;t) = \sqrt{\frac{t-x}{x}}J_1(2\sqrt{x}\sqrt{t-x}) - \sqrt{\frac{t-\Delta t-x}{x}}J_1(2\sqrt{x}\sqrt{t-\Delta t-x}), \tag{36}$$

with the understanding that these terms vanish for $x < 0$ and when $t - x < 0$ or $t - \Delta t - x < 0$. Similarly,

$$v_0(x;t) = -\frac{t-x}{x}J_2(2\sqrt{x}\sqrt{t-x}) + \frac{t-\Delta t-x}{x}J_2(2\sqrt{x}\sqrt{t-\Delta t-x}). \tag{37}$$

For small $x$ and $t > \Delta t$ we find $u_1 \approx \Delta t/\sqrt{2}$, and in this case, when the constant forcing is switched off at some point, the amplitude becomes constant near $x = 0$. Near $x = 0$, the $v_0$ field behaves like $v_0 \approx (\Delta t)^2/2 - (\Delta t)t$, and the amplitude near the forcing region grows linearly in time instead of quadratically when the forcing is switched off.

In Figure 3 we show contours of $v_0$ (Figure 3a) and of $u_1$ (Figure 3b) for the case $\Delta t = 2$. Time runs from $t = 0$ to $t = 20$, and we took $0 \le x \le 20$. We find the highest amplitudes in both panels near $x = 0$, and we find vanishingly small amplitudes near $x = t$ (the propagating fronts). These graphs show that the horizontal length scales decrease near $x = 0$ with increasing time. This is the same behavior found for the Green's function (26) shown in Figure 2 near $x = 0$. This is due to the argument $2\sqrt{x}\sqrt{t-x}$, which occurs in the Bessel functions $J_1$ and $J_2$. For small $x$ the argument is proportional to $\sqrt{xt}$, and for large $t$ this argument can cross many zeros of the Bessel functions as $x$ increases. For larger $t$ a smaller interval of $x$ values provides an equal number of zeros.

### 3.2. An Initial Value Problem

As another example, we consider the case where at $t = 0$, $u_1 = 0$ and $v_0(x; t = 0)$ are given, while the forcing remains zero at all subsequent times. According to (28), then

$$u_1(x;t) = \int_{-\infty}^{+\infty} G(x;t|x_0;0)\frac{v_0(x_0;t=0)}{\sqrt{2}}dx_0,$$

and with (20)

$$v_0(x;t) = (\partial_x + \partial_t)\int_{-\infty}^{+\infty} G(x;t|x_0;0)v_0(x_0;t=0)dx_0.$$

If we denote the Fourier spectrum of $v_0(x; t = 0)$ by $\hat{v}_0(k; t = 0)$, then the solution can be written as (see the appendix)

$$v_0(x;t) = \frac{1}{\sqrt{2\pi}}\int_{-\infty}^{+\infty} \hat{v}_0(k;t=0)F(k;t)e^{ikx}dk, \tag{38}$$

with $F$ given by (A12). For instance, consider the Gaussian initial condition

$$v_0(x;t=0) = e^{-\frac{1}{2}(x/\alpha)^2}, \tag{39}$$

where $\alpha$ determines the width of the Gaussian. Since $x$ was nondimensionalized by $L_n$ as given by (11), dimensionally, this Gaussian has an $e$-folding scale of $\alpha L_n$. The Fourier spectrum is

$$\hat{v}_0(k;t=0) = \alpha e^{-(\alpha k)^2/2}.$$

Substitution of this and (A12) in (38) gives

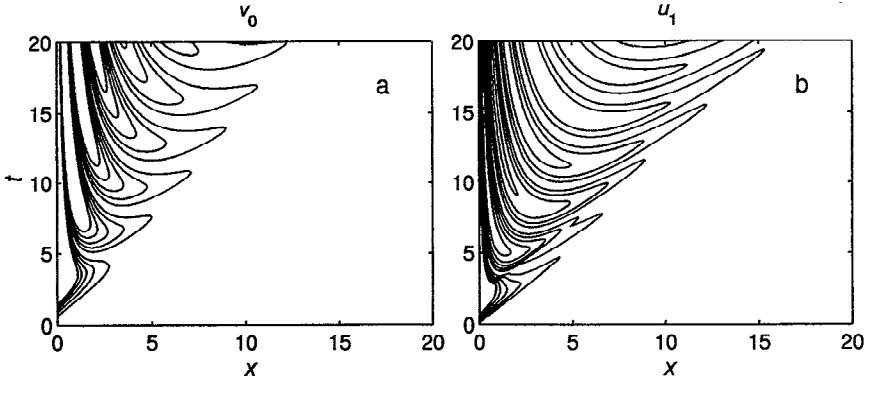


**Figure 3.** (a) The $v_0$ field and (b) the $u_1$ field in a time versus distance plot with forcing $\tau_0^y(x;t) = \delta(x)f(t)$ with $f(t)$ given by (35). The forcing is switched on at $t = 0$ and switched off at $t = \Delta t = 2$. Contour levels for $v_0$ in Figure 3a run from $-1.0$ with steps of 0.2 to 1.0. In Figure 3b the contour levels run from $-0.5$ with steps of 0.1 to 0.5. The zero contours are not shown.

$$v_0(x;t) = \frac{\alpha}{\sqrt{2\pi}} \cdot \int_{-\infty}^{+\infty} \frac{\omega_+ e^{-i\omega_- t} - \omega_- e^{-i\omega_+ t}}{\omega_+ - \omega_-} e^{-(\alpha k)^2/2 + ikx} dk, \tag{40}$$

with $\omega_\pm$ given by (16). This cannot be evaluated in closed form, but some salient features of the behavior of the solution can be found as follows. Since the exponent with $-k^2$ in it effectively kills all contributions from high $|k|$ values, we will expand the terms with $\omega_\pm$ in powers of $k$ and retain only the lowest-order ones. Thus with (16) we approximate

$$\frac{\omega_+}{\omega_+ - \omega_-} \approx \frac{1}{2} + \frac{k}{4}\left[1 - \frac{k^2}{8} + O(k^4)\right],$$
$$\frac{\omega_-}{\omega_+ - \omega_-} \approx -\frac{1}{2} + \frac{k}{4}\left[1 - \frac{k^2}{8} + O(k^4)\right],$$
$$\omega_\pm \approx \pm 1 + \frac{k}{2} \pm \frac{k^2}{8} + O(k^4).$$

Substitution in (40) gives

$$v_0(x;t) = \frac{\alpha}{2\sqrt{2\pi}} \int_{-\infty}^{+\infty} dk e^{-(\alpha k)^2/2 + ik(x-t/2)} \cdot \left\{ e^{-it}\left[1 - \frac{k}{2} + \frac{k^3}{16} + O(k^5)\right] e^{-it[k^2/8 + O(k^4)]} + e^{+it}\left[1 + \frac{k}{2} - \frac{k^3}{16} + O(k^5)\right] e^{+it[k^2/8 + O(k^4)]} \right\}. \tag{41}$$

Every occurrence of $k$ is now identified with an $x$ derivative, and up to $O(\partial_x^3)$, we get

$$v_0(x;t) = \frac{\alpha e^{-it}}{2\sqrt{2\pi}}\left[1 + \frac{i}{2}\partial_x + \frac{i}{16}\partial_x^3 + \cdots\right] \cdot \int_{-\infty}^{+\infty} e^{-k^2(\alpha^2/2 - it/8) + ik(x-t/2)} dk + \frac{\alpha e^{+it}}{2\sqrt{2\pi}}\left[1 - \frac{i}{2}\partial_x - \frac{i}{16}\partial_x^3 + \cdots\right] \cdot \int_{-\infty}^{+\infty} e^{-k^2(\alpha^2/2 + it/8) + ik(x-t/2)} dk. \tag{42}$$

The $k$ integral is easy to evaluate,

$$\frac{\alpha}{2\sqrt{2\pi}} \int_{-\infty}^{+\infty} e^{-k^2(\alpha^2/2 \pm it/8) + ik(x-t/2)} dk = \frac{\alpha}{2\sqrt{\alpha^2 \pm it/4}} e^{\frac{-(x-t/2)^2}{2(\alpha^2 \pm it/4)}},$$

and we finally have

$$v_0(x;t) = \frac{e^{-it}}{2\sqrt{1 - it/(4\alpha^2)}}\left[1 + \frac{i}{2}\partial_x + \frac{i}{16}\partial_x^3 + \cdots\right] \cdot \exp\left(\frac{-(x - t/2)^2}{2(\alpha^2 - it/4)}\right) + \text{c.c.}, \tag{43}$$

where "c.c." denotes complex conjugate. Note that for $t = 0$ the initial condition is satisfied. All higher-order corrections are odd powers of $\partial_x$. In a similar fashion, using the spectral representation for $u_1$ as discussed in the appendix, the approximate solution for $u_1$ is

$$\sqrt{2}u_1(x;t) = \frac{e^{-it}}{2i\sqrt{1 - it/(4\alpha^2)}}\left[1 + \frac{1}{2}\partial_x^2 + \cdots\right] \cdot \exp\left[\frac{-(x - t/2)^2}{2(\alpha^2 - it/4)}\right] - \text{c.c.} \tag{44}$$

For $t = 0$ the initial condition $u_1 = 0$ is satisfied. All higher-order corrections are even powers of $\partial_x$. The above leading behaviors and its corrections could alternatively have been obtained through the use of the method of steepest descent.

No matter how many of the corrective terms we keep, the $u_1$ solution (44) is symmetric about the point $x/t = 1/2$, but $v_0$ according to (43) is not. This is exactly the group velocity at $k = 0$, around where we expanded the spectral representation. The complex factor in the exponent means that the Gaussian $v_0$ distribution develops into a wavy field. The prefactor implies a simultaneous amplitude decay, which is asymptotic to $t^{-1/2}$. In Figure 4 we show the evolution of the $v_0$ field (dashed lines) where we have kept only the first correction $O(\partial_x)$ in (43). In Figure 4a the initial Gaussian is shown, with length scale $\alpha = 1$. In Figures 4b, 4c, and 4d, at times $t = 5, 10$, and 15, respectively, we see the Gaussian disperse into a wavy field, which is clearly propagating to the right. In the same figure we show the corresponding $u_1$ field (solid lines), correct to $O(\partial_x^2)$ in (44). In Figure 4a, $u_1 = 0$, but at $t = 5$, $u_1$ has developed an appreciable amplitude. In all subsequent panels we see a $u_1$ field that is symmetric about the point $x = t/2$. Contours of $v_0$ and $u_1$ are shown in Figure 5a and Figure 5b, respectively. The center of each of the innermost closed contours corresponds to a maximum amplitude. For instance, $v_0$ has a maximum at $x = 0$ when $t = 0$ then a minimum at $x \approx 3$ when $t = 2.5$, etc. Note how the maxima and minima of $u_1$ and $v_0$ alternate. The maxima and minima of $u_1$ lie exactly on the line $x = t/2$, while those of $v_0$ lie to the right of this line. Although we kept only the first corrections in the $u_1$ and $v_0$ field, it has been determined that around $t = 2$, there is an error of about 1% in the amplitudes, but at later times the error is around 0.6%, so the higher-order corrections that we discarded are unimportant.

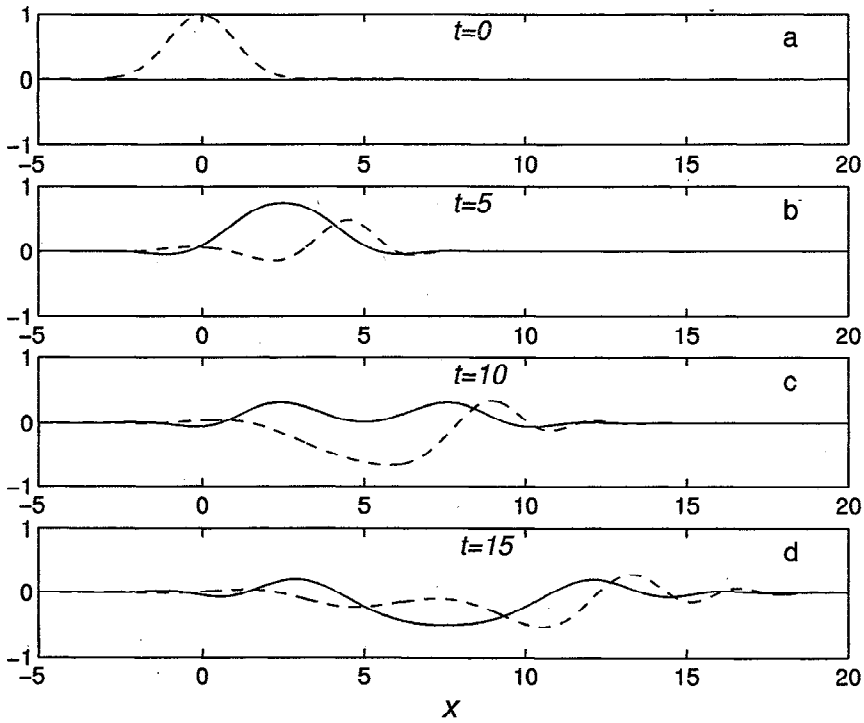


**Figure 4.** The evolution of the $v_0$ field (dashed lines), which is initially Gaussian (39) and the $u_1$ field (solid lines), which at $t = 0$ is zero. Times are as indicated. The graphs of $v_0$ show (43) only up to the $O(\partial_x)$ correction, while the graphs of $u_1$ show (44) up to the $O(\partial_x^2)$ correction.

### 3.3. Comparison With a Numerical Model

A numerical model was run to test the usefulness of the Green's function formalism presented above, using a nine-layer version of the *Gent and Cane* [1989] ocean general circulation model (CGM). For a discussion of another recent application of the same model, see *Kessler et al.* [1997]. The computation is done on an "A" grid with horizontal resolution of approximately one degree in $x$ and one-third degree in $y$. The time step is 1 hour. The initial stratification was uniform in space but representative of the tropical Pacific. The model was forced by a wind stress acting over a 26°-wide strip along the western boundary of a rectangular ocean basin. The wind was uniform in $x$ and $y$ over the strip, and the integration was started from rest. First, an eastward stress $\tau^x$ was turned on impulsively at time $t = 0$. The stress was chosen to be so weak (.01 N/m$^2$) that the model response is almost linear. The equatorial response is dominated by a series of baroclinic Kelvin waves propagating to the east and reflecting off the eastern boundary as long Rossby waves going back to the west. Plate 1 shows the results of this experiment. Plate 1a shows the upper layer $u$ field at the equator as a function of $x$ and $t$.

In order to diagnose the wave structure of the $u$ field in Plate 1a, we sought to decompose it into equatorial wave modes. This requires an initial decomposition into vertical modes (equation (7)), characterized by a speed $c_n$ and vertical eigenvector $\phi_n(z)$. It is not straightforward to perform this decomposition since the *Gent and Cane* [1989] model only resolves the upper ocean. Therefore an empirical method was used to accomplish this step, as follows. The equatorial $u$ field in the vicinity of 140°W at day 50 of the calculation was examined as a function of depth. The vertical structure, normalized by the value in the upper layer, is shown as a function of layer number in Figure 6. It is the curve which goes from 1 in layer 1 to 0.2 in layer 9, resembling a quarter period of a cosine. Since the first vertical mode Kelvin wave is the only signal we expect to see at 140°W at this time, we hypothesize that this vertical structure is the first baroclinic mode of the model. To test this idea, we projected the full model zonal current field onto this vertical mode. Plate 1 (labeled mode 1) shows this field along the equator. The expected equatorial wave behavior is apparent, including the Kelvin wave and several reflected Rossby waves. We estimated the Kelvin wave speed at 3.02 m/s for this mode. The meridional structure of the resulting $u$ field at 140°W on day 50 was Gaussian with the correct meridional scale.

The mode 1 contribution was then subtracted from the equatorial $u$ field at each point, and the entire process was repeated three more times to isolate modes 2–4. For each mode we chose a time and location in which we expected no signal other than the Kelvin wave of the mode in question. The resulting vertical structures and associated equatorial $u$ fields are also shown in Plate 1 and Figure 6. The Kelvin wave speeds for the other modes are given in the caption of Plate 1. Plate 1f is the residual upper layer equatorial $u$ field after the first four modes have been removed. This analysis pro-

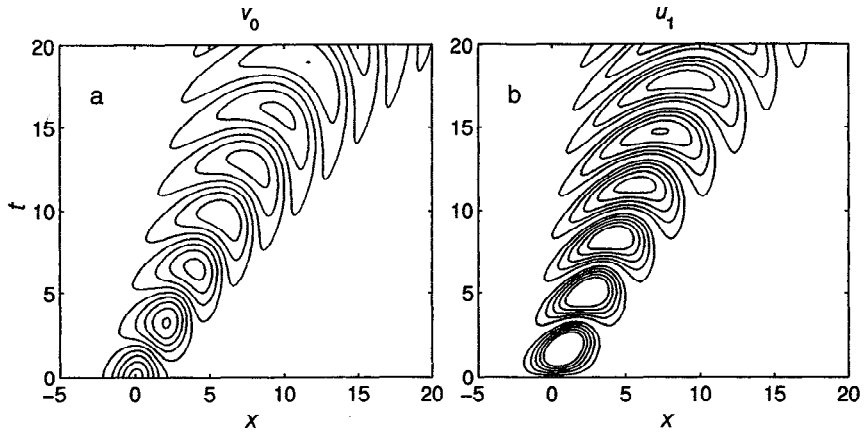


**Figure 5.** (a) The $v_0$ field and (b) the $u_1$ field in a time versus distance plot. The initial Gaussian $v_0$ field is centered around $x = 0$. Further details are given in the text. Contour levels in Figure 5a run from $-0.9$ with steps of 0.2 to 0.9. In Figure 5b the contour levels run from $-0.5$ with steps of 0.1 to 0.5. The zero contours are not shown.

vided the tools for interpreting a model run forced by a meridional stress.

The same numerical calculation was then run with a northward stress $\tau^y$. The resulting horizontal velocity fields were projected onto the empirical vertical modes determined in the previous calculation. The resulting meridional velocity field $v$ was projected onto the Hermite function $\psi_0(y/L_n)$ given by (13) for each mode, where $L_n$ is the equatorial Rossby radius for the vertical mode in question on the basis of the empirically determined Kelvin wave speed for that mode (see (11)). In this way the mixed Rossby gravity wave response for each mode was isolated.

Plate 2b shows the $(x, t)$ structure of the meridional velocity $v_0$ of the first baroclinic mode mixed Rossby-gravity wave in the GCM run, as determined above. Within the forcing region on the left side of the figure the response shows a series of roughly hyperbolic bands, which persist for about 150 days and then disappear. A pronounced signal persists near the two edges of the forcing region throughout the yearlong integration. To the east of the forcing region, there is a more complicated banded structure exhibiting some sort of interference pattern. Two "null" wedges are apparent in the graph, one reaching the eastern boundary around day 180 and the other around day 300. The banded structure changes sign across the null wedges, indicating a modulation of the spreading wave pattern. Notice that there are no eastern boundary reflections apparent in this diagram. The projection of $v$ onto the lowest Hermite mode $\psi_0$ filters out the Rossby waves that constitute the reflection of the mixed Rossby gravity wave.

For the first baroclinic mode the Kelvin wave speed $c_1$ is about 3 m/s, so a signal from the eastern edge of the forcing could cross the basin in 50 days. The mixed Rossby gravity wave signal appears at the eastern boundary around day 90, traveling considerably slower than $c_1$ but slightly faster than $c_1/2$. During the period the model was run it appears that for values of $x$ between the edge of the forcing region and roughly 150°W the response dies out after some time.

We would like to explain each of these features based on the linear theory we have outlined above and the properties of the numerical model used in the simulation. Thus we investigate the $v_0$ response to switched-on forcing with uniform amplitude in a strip of nondimensional width $\Delta$. We focus our attention here on the response with respect to the first vertical normal mode. The numerical model had a 26-degree-wide forcing strip, which corresponds for the first vertical normal mode to a forcing strip of width $8L_1$. Thus, in the linear theory, we take $\tau_0^y = f(x)U(t)$ with

$$\begin{aligned} f(x) &= 1, \quad 0 \le x < \Delta, \\ f(x) &= 0, \quad x > \Delta, \end{aligned} \tag{45}$$

with $\Delta = 8$. The answer can be written in the following form,

$$\begin{aligned} v_0(x;t) &= -\int_0^x \frac{f(x_0)}{2\pi i} \int_{c-i\infty}^{c+i\infty} \frac{e^{st-(s+s^{-1})(x-x_0)}}{s^3} ds dx_0 \\ &\quad + f(x)t \\ &= -\int_0^x f(x_0) \frac{t-(x-x_0)}{x-x_0} \\ &\quad \cdot J_2\left[2\sqrt{x-x_0}\sqrt{t-(x-x_0)}\right] dx_0 + f(x)t. \end{aligned} \tag{46}$$

Because of (45) the second term is zero outside the forcing strip, i.e., for $x > \Delta$, while in that case, the $x_0$ integral has as an upper integration limit $x_0 = \Delta$. This expression may be compared with (34), where the switch-on forcing was concentrated in $x$; that is, $\tau_0^y = \delta(x)U(t)$. Both in (34) and (46) the second term gives the directly forced response of the $v_0$ field; that is, in both cases

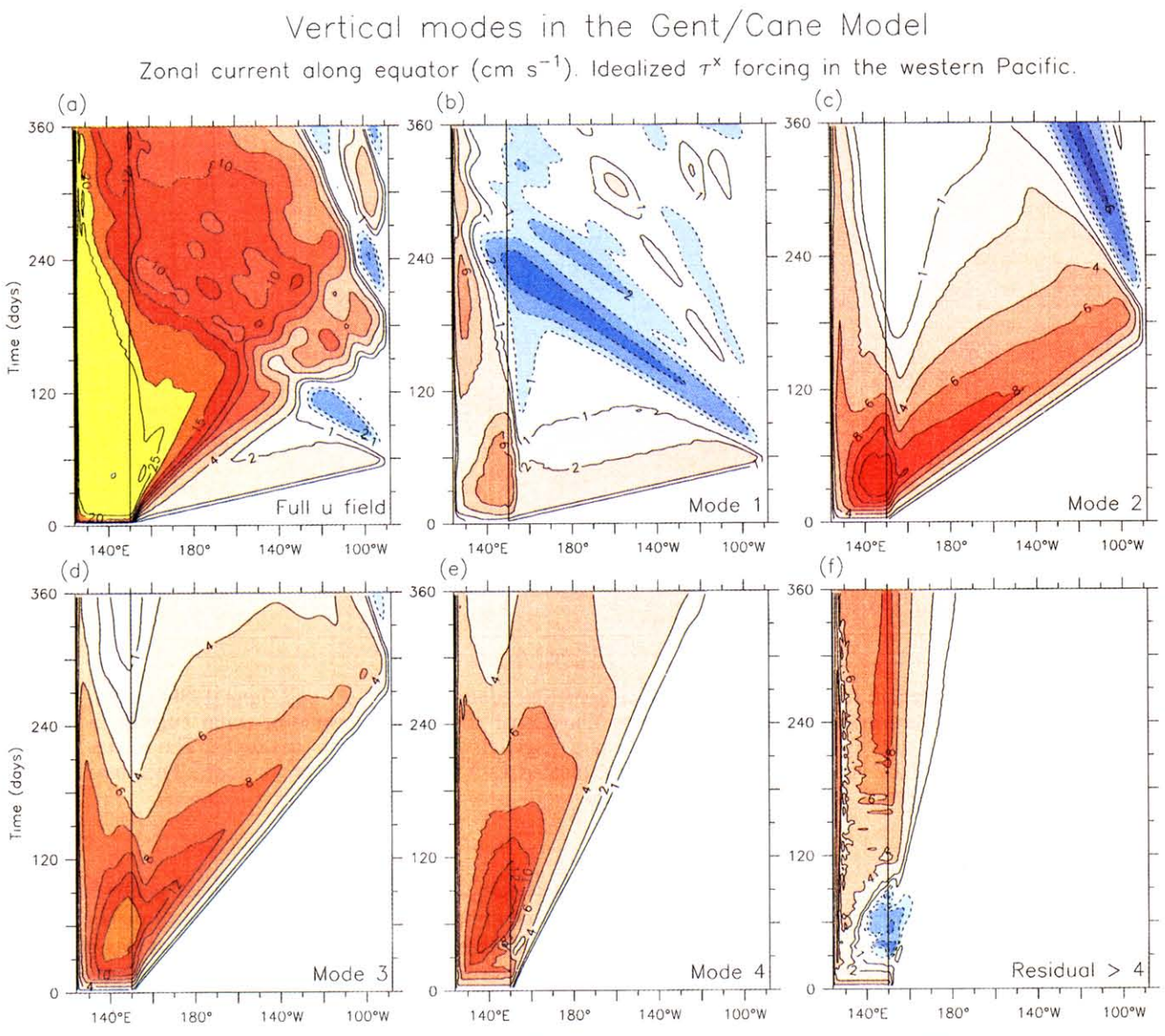


**Plate 1.** The $u$ field (cm/s) due to a uniform zonal wind stress acting over a 26°-wide strip next to the western boundary of a rectangular ocean basin in a nine-layer versic *and Cane* [1989] general circulation model. (a) Full surface $u$ field at the equat equatorial $u$ field for the first four vertical modes, labeled in the lower right corner The Kelvin wave speeds for these modes are $c_1 = 3.02$ m/s, $c_2 = 0.99$ m/s, $c_3 =$ $c_4 = 0.30$ m/s. (f) Residual surface $u$ field at the equator. For further details, see

these terms correspond to $v_0(x;t) = \int_0^t \tau_0^y(x;t')dt'$. The first term of (46) is seen to be equal to an integral over the oscillatory part of the response due to point-source forcing.

The integral over $x_0$ was numerically determined. The result is shown in Plate 2a. It has been plotted for a nondimensional time period of 250, which corresponds for the first vertical mode to 348 days. The length of vertical axis in Plate 2a has been made slightly shorter than in Plate 2b to account for the difference with the 360-day period used in the numerical model. The size of the domain to the right of the forcing strip is 37.2 units, which corresponds to the longitude band of 122° wide used in the numerical model. As in the GCM results, this solution shows the presence of null wedges in the region east of the forcing. Referring to (46), we see that the field outside the forcing strip shown in Plate 2a can be interpreted as an interference pattern resulting from the superposition of the wave fields due to sources continuously distributed over the length of the strip.

The wedges seen in Plate 2 can be accounted for with asymptotic analysis. For $x > \Delta$ (outside the forcing strip) we perform the $x_0$ integral first in (46) and find

$$v_0(x;t) = -\frac{1}{2\pi i}\int_{c-i\infty}^{c+i\infty} g(s)e^{st-(s+s^{-1})(x-\Delta/2)}ds, \quad (47)$$

where

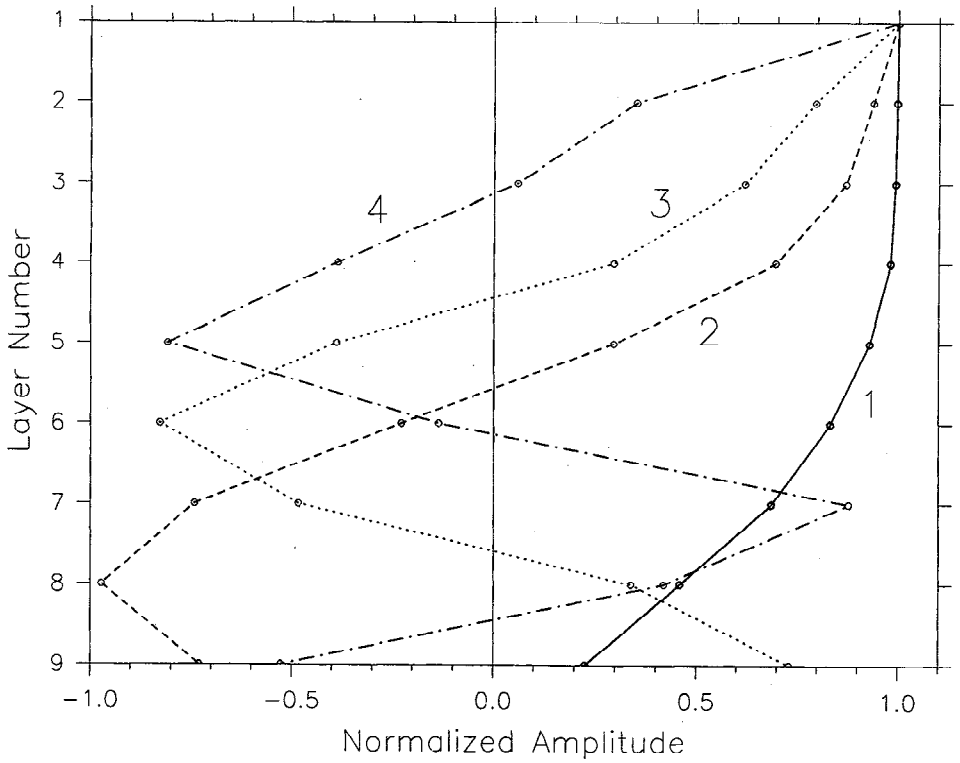


**Figure 6.** Vertical structure of the first four baroclinic modes of the *Gent and Cane* [1989] model. The modes were determined empirically by diagnosing the vertical profile of zonal current in regions where the variability consisted solely of a single-mode Kelvin wave (see text). The modes are normalized by the surface amplitude and plotted as a function of layer number. The total thickness of layers 1 through 9 is about 400 m.

$$g(s) = \frac{e^{(s+s^{-1})\Delta/2} - e^{-(s+s^{-1})\Delta/2}}{s^2(s^2+1)}. \tag{48}$$

For $t > x - \Delta$ the $s$ contour can be deformed into the left-hand side of the complex $s$ plane. It would appear that in the process of doing so, two poles at $s \pm i$ occurring in $g(s)$ are enclosed, but further analysis shows that these give no contribution to the integral. By defining

$$s = as', \quad a = \frac{\sqrt{x-\Delta/2}}{\sqrt{t-(x-\Delta/2)}}, \tag{49}$$

(47) becomes

$$v_0(x;t) = -\frac{a}{2\pi i}\int_{c-i\infty}^{c+i\infty} g(s')e^{\sqrt{x-\Delta/2}\sqrt{t-(x-\Delta/2)}(s'-s'^{-1})}ds', \tag{50}$$

where $g(s')$ is as in (48) but with (49) substituted. The substitution (49) is a mere stretching of the $s$ plane, and the contour in the $s'$ plane is as the original $s$ contour. Assuming that

$$\lambda = \sqrt{x-\Delta/2}\sqrt{t-(x-\Delta/2)} \tag{51}$$

is large, we can apply the method of steepest descent to get approximations to (50) [see *Bleistein and Handelsman,* 1975]. The stationary phase points in the $s'$ plane are at $s' = \pm i$. The function $g(s')$ does not vanish at these points, except for special values of $x$ and $t$. In order to avoid a discussion of any unnecessary details we remark merely that the original contour can be deformed to run in the directions of steepest descent at the stationary phase points. It takes a deformation into the left half plane of the complex $s'$ plane. To the leading order in the large parameter $\lambda$ (51) we find

$$v_0(x;t) \approx \frac{2\sin\left[(a-a^{-1})\Delta/2\right]}{\sqrt{\pi\lambda}a(a^2-1)}\sin(2\lambda - 3\pi/4). \tag{52}$$

This leading order behavior vanishes when

$$(a - a^{-1}) = \frac{2n\pi}{\Delta}, \tag{53}$$

or when

$$\frac{t}{x-\Delta/2} = 1 + \left(\frac{n\pi}{\Delta} + \sqrt{1+\frac{n^2\pi^2}{\Delta^2}}\right)^2, \quad |n| = 0, 1, 2, \cdots \tag{54}$$

The right-hand side defines for every $n$ a slope of a straight line in the $xt$ plane (with an apparent origin in the middle of the forcing region $x = \Delta/2$) along which for large argument $\lambda$ the leading order term vanishes. For $n = 1$ we find this slope to be 3.15, and for $n = 2$ the

slope is 5.23. These values correctly predict the slope of the wedges seen in Plates 2a and 2b.

An interesting difference between the numerical and analytic results is seen near the edges of the forcing region in Plate 2. Since the strength of the forcing changes discontinuously across the edge of the strip, the resulting $v_0$ field has a discontinuity as well, and the size of this discontinuity grows linearly with time. Thus we find in the analytic solution a $v_0$ field that is large and discontinuous in $x$. The numerical model of *Gent and Cane* [1989] uses a Shapiro filter in space to smooth the various fields. This primarily damps out short-scale waves. Near the edges of the forcing region this produces a $v_0$ field, which becomes steady in time, rather than growing and oscillating as the linear theory predicts. Furthermore, the effect of this smoothing near the edges of the forcing propagates eastward. This accounts for the fact that in the numerical model calculation after a finite time the $v_0$ field at each $x$ dies out, except near the edges of the forcing. This may also account for the fact that in Plate 2b, only two of the null wedges are visible, while in Plate 2a, six null wedges can be seen. To get a comparable effect in the analytic model, some explicit frictional process would have to be included. Otherwise, the inviscid solution continues to grow and develop shorter and shorter $x$ scales near the boundary, just as discussed at the end of section 3.1. (Also see *Lighthill* [1969].)

## 4. Summary and Discussion

We have derived a Green's function (26) with which the mixed Rossby gravity wave response due to arbitrary forcing can be determined. With respect to a given vertical mode the evolutions of the zonal and meridional velocity are determined by their initial values and the time history of the forcing. On a domain of infinite extent in the zonal direction $x$ the exact expressions are (28) and (29). In the presence of a western boundary these expressions are modified by additional terms given in section 2.3. In that case, in order to uniquely determine the eastward propagating mixed Rossby gravity wave signal, the time history of the zonal and meridional velocity at the boundary needs to be provided. In section 3 a few analytical examples have been given, which show that the discontinuous behavior of the Green's function at the leading edge, which propagates with the maximum group velocity, disappears when switched-on forcing or an initial condition of finite size is used. In section 3.3 we have shown that the Green's function representation for the solution of forced mixed Rossby gravity waves enables us to make predictions about the ocean response that compare well with the results of an oceanic general circulation numerical model.

The analytic solutions help account for features of the general circulation model output which would be difficult to interpret by less complete descriptions of the physics. The agreement between the analytic and numerical results is quite good over most of the $(x, t)$ domain. In the regions where they do not agree, there are plausible explanations for the disagreement.

An additional numerical model experiment was run with the forcing confined to a strip in the middle of the basin. The results in the forcing region and to the east of it were virtually unchanged. Thus we conclude that for this particular example, very little energy goes into long Rossby waves propagating westward. Such long Rossby waves reflecting from the western boundary could in theory generate additional mixed Rossby gravity waves but did not appear to do so in our year-long integration.

A word of caution may be in order. Analysis in terms of equatorial wave theory is fairly straightforward when all the fields are available. In particular, the meridional velocity provides the basic description of the various waves that can occur, through (12), by which any $v$ field can be uniquely decomposed into meridional modes $\psi_m$. The Kelvin wave must of course be discussed separately since it has no $v$ field (at least on the equatorial beta plane). On the other hand, the pressure and zonal current fields by themselves are more difficult to analyze. Projecting onto vertical modes $\phi_n(z)$ and then projecting onto Hermite functions does not directly provide an unambiguous result. A $p$ field or $u$ field proportional to the Hermite function of order $m$ can be associated with $v$ fields of order $m+1$ or order $m-1$. One needs the projection of $u_n + p_n/c_n$ and $u_n - p_n/c_n$ on $\psi_m(y/L_n)$ to sort this out completely [*Gill and Clarke*, 1974; *Gill*, 1982, section 11.4]. If one has $p$ but not $u$ or $v$, the problem is harder. In particular, application of these ideas to the analysis of altimeter data may not be easy.

## Appendix: Green's Function

Solutions to (18) and (21) can be expressed in a general fashion with the use of an appropriate Green's function. The conjugate equations of (18) and (21) for the Green's function $G$ is

$$\partial_{t_0}^2 G + \partial_{t_0}\partial_{x_0} G + G = \delta(t - t_0)\delta(x - x_0), \qquad \text{(A1)}$$

where the $\delta$ values are Dirac delta functions. The Green's function is a function of two sets of independent variables $G = G(x; t|x_0; t_0)$, where the space-time variables with an index 0 are "source coordinates" and the ones without are "observer coordinates." Causality is ensured by imposing that $G$ and its derivatives are zero for $t_0 > t$. Also, on the infinite domain, we want $G$ to vanish for $|x - x_0| \to \infty$. There are various ways to solve (A1). We employ the following method here, which is useful when solving an initial value problem like the one presented in section 3.2. We look for a spectral representation of $G$ of the form

$$G(x; t|x_0; t_0) = \frac{1}{2\pi} \int_{-\infty}^{+\infty} \int_{-\infty}^{+\infty} g(k, \omega) e^{ik(x-x_0) - i\omega(t-t_0)} dk d\omega.$$

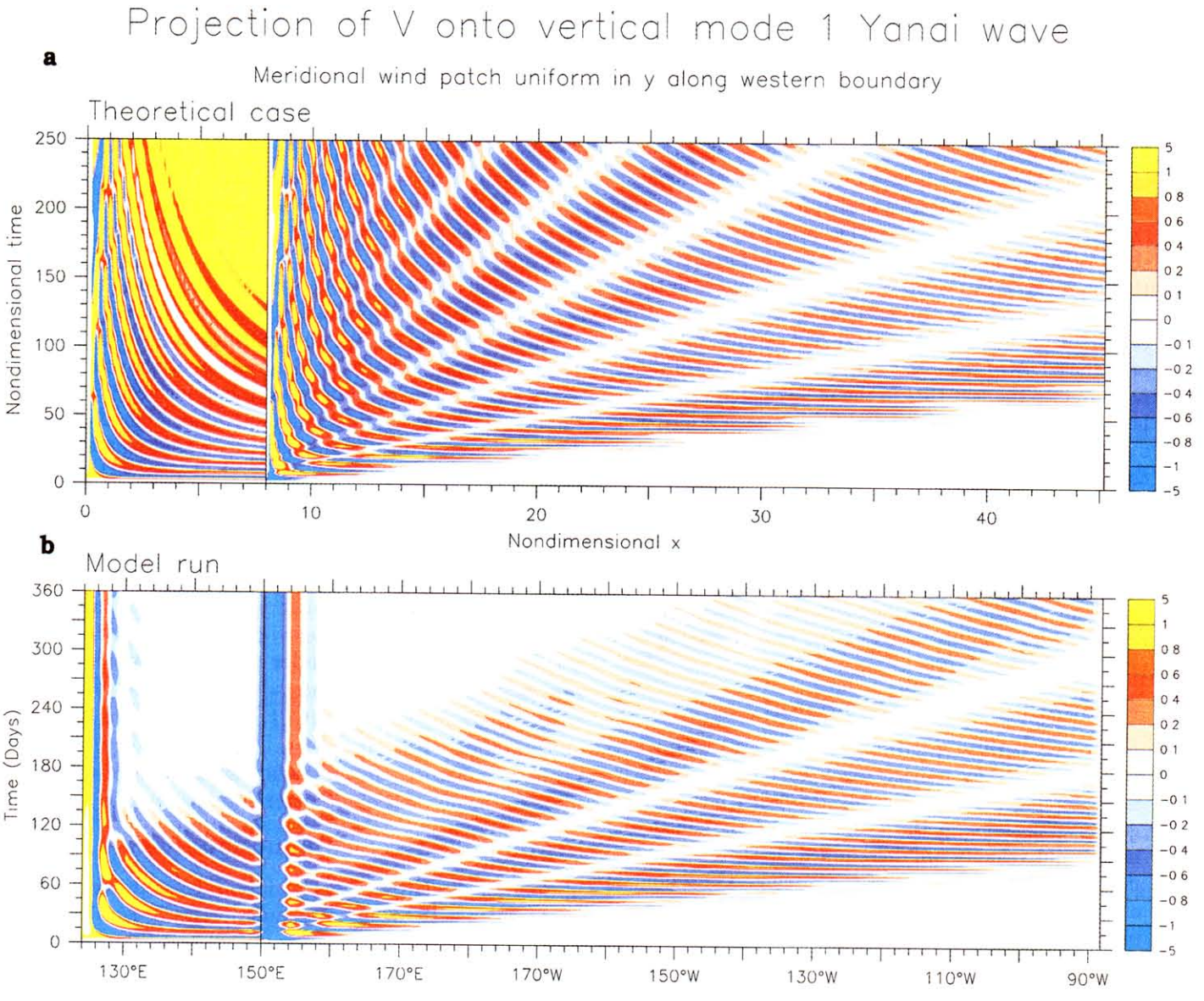


**Plate 2.** The mixed Rossby gravity $v_0$ field associated with the first vertical mode (due to a forcing $\tau^y$ that is uniform in a strip of 26° longitude or $8L_1$ wide) on the western side of the ocean basin (forcing edge shown by vertical line). The forcing is switched on at day 0 or $t = 0$ and remains constant thereafter. (a) Theoretical solution (equation (46)) where the units of distance and time are $L_1$ and $T_1$ (equation (11)), respectively; (b) General circulation model (GCM) solution, with corresponding units of degrees longitude and days. The model solution is shown for the first 360 days, while the theoretical solution is shown for $250T_1$, which corresponds to about 348 days; Plate 2a is slightly shorter to account for this difference. The zonal extent of both fields are the same. The model values are in cm/s. The theoretical solution is nondimensional; for the unit forcing we used, the values coincidentally have similar amplitude to the model solution.

(A2)

Furthermore, we use the well-known Fourier representation for delta functions [*Morse and Feshbach*, 1953]

$$\delta(x - x_0) = \frac{1}{2\pi}\int_{-\infty}^{+\infty} e^{ik(x-x_0)}dk,$$

$$\delta(t - t_0) = \frac{1}{2\pi}\int_{-\infty}^{+\infty} e^{-i\omega(t-t_0)}d\omega. \qquad \text{(A3)}$$

Substitution in (A1) shows that

$$g(k,\omega) = \frac{1}{2\pi(-\omega^2 + k\omega + 1)} = \frac{-1}{2\pi(\omega - \omega_+)(\omega - \omega_-)}, \qquad \text{(A4)}$$

where $\omega_\pm$ are the two solutions given by the dispersion relation (16) for a given $k$. If we want to perform the $\omega$ or $k$ integral, we run into the usual situation that there is some ambiguity as to how to evaluate the integrals because there are poles on the real $\omega$ axis for fixed $k$ and vice versa. This is often circumvented by introducing either a small dissipative term to the system, which moves poles off the real axis [*Lighthill*, 1978], or by suitably defining the delta functions as a limit of a well-behaved function. For instance, if we add some Rayleigh damping to the right-hand side of (8)–(10), i.e., terms $-\varepsilon u_n$, $-\varepsilon v_n$, and $-\varepsilon p_n$, respectively, then the dispersion relation becomes

$$\omega_\pm(k) = -i\varepsilon + \frac{k}{2} \pm \sqrt{1 + \frac{k^2}{4}}. \qquad \text{(A5)}$$

Now the $\omega$ integral for fixed $k$ is easily determined. The poles at $\omega = \omega_\pm$ lie in the lower half of the complex plane. Substituting (A4) in (A2) and performing the $\omega$ integral, we find that the integral is zero for $(t - t_0) < 0$ by closing the contour in the upper half plane, and for $t - t_0 > 0$ the integral is evaluated by closing in the lower half plane. This encircles the poles in negative direction, and we get

$$G(x;t|x_0;t_0) = U(t - t_0)\int_{-\infty}^{+\infty} G(k;t - t_0)e^{ik(x-x_0)}dk, \qquad \text{(A6)}$$

with

$$G(k;t) = \frac{e^{-i\omega_-(k)t} - e^{-i\omega_+(k)t}}{i[\omega_+(k) - \omega_-(k)]}, \qquad \text{(A7)}$$

with $\omega_\pm$ as in (A5). The causality is enforced by the damping term. It kills all waves due to sources at time $t - t_0 = -\infty$; that is, all the waves that are solutions to the homogeneous part of (A1). The limit $\varepsilon \downarrow 0$ can now be taken in (A7). With some elementary transformations, (A6) can next be brought to the form (26).

The spectral form of $G$ in (A7) is useful for initial value problems where the $k$ spectrum of $u_1$ and $v_0$ is given. For instance, if $u_1(x;t = 0) = 0$ and $v_0(x;t = 0) \neq 0$, then for $t > 0$ we find with (28) and subsequent use of the convolution theorem for Fourier transforms

$$u_1(x;t) = \int_{-\infty}^{+\infty} G(x;t|x_0;t_0 = 0)\frac{v_0(x_0;t = 0)}{\sqrt{2}}dx_0 = \frac{1}{\sqrt{2\pi}}\int_{-\infty}^{\infty} \frac{\hat{v}_0(k;t = 0)}{\sqrt{2}}G(k;t)e^{ikx}dk, \qquad \text{(A8)}$$

where

$$\hat{v}_0(k;t = 0) = \frac{1}{\sqrt{2\pi}}\int_{-\infty}^{+\infty} v_0(x;t = 0)e^{-ikx}dx. \qquad \text{(A9)}$$

More generally, if we denote the Fourier transforms (in $x$) of $u_1(x;t)$ and $v_0(x;t)$ by $\hat{u}_1(k;t)$ and $\hat{v}_0(k;t)$, respectively, we get

$$\hat{u}_1(k;t) = \hat{u}_1(k;t = 0)F(k;t) + \left[\hat{v}_0(k;t = 0)/\sqrt{2} - ik\hat{u}_1(k;t = 0)\right]G(k;t), \qquad \text{(A10)}$$

$$\hat{v}_0(k;t) = \hat{v}_0(k;t = 0)F(k;t) - \sqrt{2}\hat{u}_1(k;t = 0)G(k;t), \qquad \text{(A11)}$$

where

$$F(k;t) = (ik + \partial_t)G = \frac{\omega_+(k)e^{-i\omega_-(k)t} - \omega_-(k)e^{-i\omega_+(k)t}}{\omega_+(k) - \omega_-(k)}. \qquad \text{(A12)}$$

**Acknowledgments.** The authors thank the reviewers for their helpful comments and Greg Johnson (PMEL/NOAA) for help in using a numerical program. This paper is funded in part by cooperative agreement NA37RJ0199 from the National Oceanic and Atmospheric Administration. Contribution 1889 from NOAA/Pacific Marine Environmental Laboratory.

## References

Blandford, R., Mixed Rossby gravity waves in the ocean, *Deep Sea Res. Oceanogr. Abstr., 13,* 941–961, 1966.

Bleistein, N., and R. A. Handelsman, *Asymptotic Expansions of Integrals*, Dover, Mineola, N. Y., 1975.

Cane, M. A., and E. S. Sarachik, Forced baroclinic ocean motions, I, The linear equatorial unbounded case, *J. Mar. Res., 34,* 629–665, 1976.

Cane, M. A., and E. S. Sarachik, Forced baroclinic ocean motions, II, The linear equatorial bounded case, *J. Mar. Res., 35,* 395–432, 1977.

Cane, M. A., and E. S. Sarachik, The response of a linear baroclinic equatorial ocean to periodic forcing, *J. Mar. Res., 39,* 651–693, 1981.

Enfield, D. B., M. del Pilar Cornejo-Rodriguez, R. L. Smith, and P. S. Newberger, The equatorial source of propagating variability along the Peru coast during the 1982–1983 El Niño, *J. Geophys. Res., 92,* 14,335–14,346, 1987.

Gent, P. R., and M. A. Cane, A reduced gravity, primitive

equation model of the upper equatorial ocean, *J. Comput. Phys., 81,* 444–480, 1989.

Gill, A. E., *Atmosphere-Ocean Dynamics*, 661 pp., Academic, San Diego, Calif., 1982.

Gill, A. E., and A. J. Clarke, Wind induced upwelling, coastal currents and sea level changes, *Deep Sea Res. Oceanogr. Abstr., 21,* 325–345, 1974.

Kessler, W. S., L. M. Rothstein, and D. Chen, The annual cycle of SST in the eastern tropical Pacific, as diagnosed in an ocean GCM, *J. Clim.*, in press, 1998.

Kindle, J. C., and J. D. Thompson, The 26- and 50-day oscillations in the western Indian Ocean: Model results, *J. Geophys. Res., 94,* 4721–4736, 1989.

Lighthill, M. J., Dynamic response of the Indian Ocean to the onset of the Southwest Monsoon, *Philos. Trans. R. Soc. London A, 265,* 45–93, 1969.

Lighthill, M. J., *Waves in Fluids*, Cambridge Univ. Press, New York, 1978.

Luyten, J. R., and D. H. Roemmich, Equatorial currents at semi-annual period in the Indian Ocean, *J. Phys. Oceanogr., 12,* 406–413, 1982.

Matsuno, T., Quasi-geostrophic motions in equatorial areas, *J. Meteorol. Soc. Jpn., 44,* 25–43, 1966.

McCreary, J. P., Eastern tropical ocean response to changing wind systems with applications to El Niño, *J. Phys. Oceanogr., 6,* 632–645, 1976.

McCreary, J. P., A linear stratified ocean model of the equatorial undercurrent, *Philos. Trans. R. Soc. London A, 298,* 603–635, 1981.

McCreary, J. P., A model of the tropical ocean-atmosphere interaction, *Mon. Weather Rev., 111,* 370–389, 1983.

McCreary, J. P., Equatorial beams, *J. Mar. Res., 42,* 395–430, 1984.

McCreary, J. P., Modeling equatorial oceanic circulation, *Annu. Rev. Fluid Mech., 17,* 359–409, 1985.

Moore, D. W., Planetary-gravity waves in an equatorial ocean, Ph.D thesis, Harvard Univ., Cambridge, Mass., 1968.

Moore, D. W., and J. P. McCreary, Excitation of intermediate-frequency equatorial waves at a western ocean boundary: With application to observations from the Indian Ocean, *J. Phys. Oceanogr., 95,* 5219–5231, 1990.

Moore, D. W., and S. G. H. Philander, Modelling of the tropical ocean circulation, in *The Sea*, vol. 6, *Marine Modelling*, edited by E. D. Goldberg et al., pp. 319–361, Wiley-Interscience, New York, 1977.

Morse, P. M., and H. Feshbach, *Methods of Theoretical Physics*, McGraw-Hill, New York, 1953.

Reverdin, G., and J. Luyten, Near-surface meanders in the equatorial Indian Ocean, *J. Phys. Oceanogr., 16,* 1088–1100, 1986.

Ripa, P., and S. P. Hayes, Evidence of equatorial trapped waves at the Galapagos Islands, *J. Geophys. Res., 86,* 6509–6516, 1981.

Rossby, C. G., Relation between variations in the intensity in the zonal circulation of the atmosphere and the displacements of the semi-permanent centers of action, *J. Mar. Res., 2,* 38–55, 1939.

Tsai, P. T. H., J. J. O'Brien, and M. E. Luther, The 26-day oscillation observed in the satellite sea surface temperature measurements in the equatorial western Indian Ocean, *J. Geophys. Res., 97,* 9605–9618, 1992.

Watson, G. M., *Theory of Bessel Functions,* Cambridge Univ. Press, New York, 1966.

Weisberg, R. H., and A. M. Horigan, Low-frequency variability in the equatorial Atlantic, *J. Phys. Oceanogr., 11,* 913–920, 1981.

Wiener, N., *The Fourier Integral and Certain of its Applications,* Cambridge Univ. Press, New York, 1933.

W. S. Kessler and D. W. Moore, Pacific Marine Environmental Laboratory, NOAA, 7600 Sand Point Way NE, Seattle, WA 98115. (e-mail: moore@pmel.noaa.gov)

R. C. Kloosterziel, School of Ocean and Earth Science and Technology, University of Hawaii, Honolulu, HI 96822.

(Received November 4, 1996; revised July 29, 1997; accepted August 28, 1997.)